2022-01-0401 Published 29 Mar 2022



A Simulation Study on the Transient Behavior of a Gasoline Direct Injection Engine under Cold Start Conditions

Delong Li, Jinghu Hu, Matthew Hall, and Ron Matthews The University of Texas at Austin

Citation: Li, D., Hu, J., Hall, M., and Matthews, R., "A Simulation Study on the Transient Behavior of a Gasoline Direct Injection Engine under Cold Start Conditions," SAE Technical Paper 2022-01-0401, 2022, doi:10.4271/2022-01-0401.

Received: 24 Jan 2022 Revised: 24 Jan 2022 Accepted: 24 Jan 2022

Abstract

he cold start process is critical to control the emissions in a gasoline direct injection (GDI) engine. However, the optimization is very challenging due to the transient behavior of the engine cold start. A series of engine simulations using CONVERGE CFD™ were carried out to show the detailed process in the very first firing event of a cold start. The engine operating parameters used in the simulations, such as the transient engine speed and the fuel rail pressure (FRP), came from companion experiments. The cylinder pressure traces from the simulations were compared with experiments to help validate the simulation model. The effects of variation of the transient parameters on in-cylinder mixture distribution and combustion are presented, including the effects of the rapidly changing engine speed, the slowly vaporized fuel due to the cold walls, and the low FRP during the first firing cycle of a 4-cylinder engine. Comparison was also made with non-transient steady state operation. It was shown that the injection-induced tumble ratio in the cylinder varied for different engine speed cases, resulting in a better fuel distribution in the low engine speed case. A relatively high turbulence level during the combustion process was seen in the transient engine speed case that led to strengthened combustion. The fuel tracking from the simulation indicated that about 30% of the fuel remained unreacted at a very late crank angle, in which 8% was in the gas phase and 22% in the liquid phase as wall films. As the FRP increased, the fuel droplets became smaller, and more fuel vaporized before hitting the piston. But the splash and rebound fuel fraction off the piston bowl was even less, resulting in a lower overall gas-phase equivalence ratio in the first firing event for the high FRP case. On the other hand, the fuel distribution was more homogeneous under the high FRP condition due to the high injection velocities. There should be an optimal FRP value, but it was difficult to discern since the peak pressures in different FRP cases were similar and turbulence levels varied in a non-monotonic way, as well, which would lead to cycle-to-cycle variations in the real engine.

Introduction

ooking to the future, cold start emissions have become one of the major concerns for manufacturers of automotive internal combustion engines. To meet the increasingly more stringent emissions standards, considerable effort has been focused on improving the cold start processes in both gasoline direct injection (GDI) and port-fuel injection (PFI) engines.

GDI engines continue to increase their market share, and have shown many benefits over PFI engines, the most important of which is the better fuel economy (up to 25% potential improvement [1]). In a GDI engine, the fuel is delivered directly into the cylinder using a higher injection pressure. This abates problems related to the port fuel films in a PFI engine [2]. However, the cold start emissions, especially hydrocarbon (HC) emissions, remain a key problem for GDI engines [3]. More than 80% of total tailpipe HC emissions come from the cold start transient processes in the Federal Test Procedure (FTP) [4].

Cold start is a start-up process in an engine where the coolant and ambient temperatures are roughly the same. More fuel has to be injected during the first several cycles of cold start to compensate for the low evaporation rate due to the low temperature. At the same time, the fuel rail pressure (FRP) increases from the lift pump pressure to the desired injection pressure but is still much lower than the normal working pressure [5]. The low FRP will lead to relatively poor atomization [6]. The unevaporated fuel will hit the cold wall and form a liquid film, and then continue to evaporate. The unevaporated fraction will remain as the film, hide in the crevices of the engine, or get absorbed into the oil films and the deposits, escaping the combustion process and resulting in more engineout hydrocarbon emissions. Moreover, the temperature of the catalysts used in the after-treatment systems will be below their light-off temperature. Hence these systems cannot be fully operational, and high levels of HCs will be exhausted to the atmosphere [7]. The current solutions to improve cold start emissions fall into the following two categories [8]: optimizing

the basic design and control strategy to improve the engine-out emissions, which is the focus of this research, and improving the exhaust after-treatment system [2, 10].

Both experiments ([11-14]) and simulations ([15-18]) have been concentrated on the first several cold start cycles to study what happens in the combustion processes and what can be done for further improvements. In cold start experiments, a goal of the researchers is to keep the engine cold and eliminate wall fuel films before each experiment, which can introduce some extra work and difficulties, the most important of which is that only one cold start experiment can be performed each day, in general. Computational fluid dynamic (CFD) methods prove then to be a useful and promising tool to visualize the overall process, including gas flow, fuel injection and vaporization, combustion of the mixture, etc., providing insights for further improvements.

Xu et al. [15] used the Ford in-house CFD code to study the cold start performance of a GDI engine. They analyzed the effects of injection timing and fuel pressure at three different engine speeds (RPM=200, 500, and 1200) and also studied the effects of piston bowl designs. Malaguti [16] et al. used the three-dimensional CFD code, Star-CD, to investigate the fuel-air mixture preparation and fuel film formation at different ambient temperatures during engine cold start processes. Ravindran et al. [17] modified the G-Equation flamelet model to improve the model capabilities to predict the direct injection spark ignition (DISI) engine performance under cold start conditions. Kim et al. [18] focused on the mixture formation for different engine conditions by also using Star-CD. They optimized the injection strategy and compared the results with their engine test results. Different constant engine speeds were used in these papers to simulate the cold start conditions in different engines. However, the engine speed can change dramatically for the first firing cycle of the first cylinder that fires to the second that fires, and so on during the first firing cycles of the cold start process. The transient engine speed will introduce more challenges to cold start simulations and will also show different behavior from the constant engine speed cases.

The first several firing cycles will be the most important in controlling cold start emissions due to the transient behavior and the low fuel rail pressure and engine temperature. Only the very first firing event of the cold start of a GDI engine, which has the worst environment, is considered in this paper. A three-dimensional commercial software package, CONVERGE CFD™, was utilized to expand the understanding of how the engine responds to the transient engine speed and to the low fuel rail pressure under these conditions. The temporal engine speed from the cold start experiments was used in all of the simulations except for the specified cases with constant speeds used for comparison. The fuel was tracked once injected. The mixture formation and the mixture motion were studied in detail to show the importance of vapor pressure. Validations and comparisons with experiments were made.

Engine Configuration

A Ford 2017-model-year 4-cylinder 2.0-liter gasoline turbocharged direct injection (GTDI) engine was used in this

TABLE 1 Engine specifications.

Engine Specifications	Details
Type	4-stroke GDI engine
Displacement (cc)	1999
Bore / Stroke (mm)	87.5 / 83.1
Connecting Rod Length (mm)	155.9
Compression Ratio	10:1
IVO (degrees ATDC)	10.9
IVC (degrees ABDC)	71.1
EVO (degrees BBDC)	55.1
EVC (degrees ATDC)	5.1
Injector	6-hole injector
Start of early injection (degrees BTDC)	220
End of late injection (degrees BTDC)	45
Fuel	Gasoline
Firing order	3-4-2-1

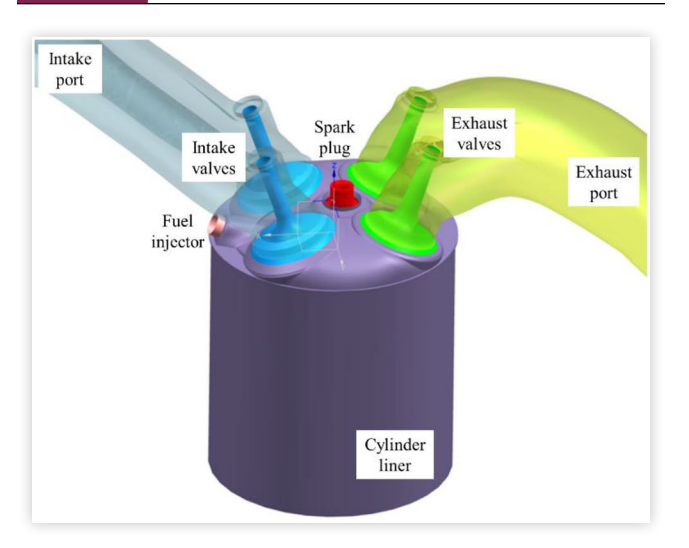
research. The specifications of the engine are listed in <u>Table 1</u>. The engine has four cylinders with two intake valves and two exhaust valves per cylinder, and the compression ratio was 10:1. The bore was 87.5 mm, and the stroke 83.1 mm. The engine had a six-hole fuel injector with operational fuel pressure up to 200 bar. A dual injection strategy was used in the cold start process, with an early injection during the intake stroke to provide a homogeneous fuel-air mixture, serving as the background fuel vapor in the cylinder, and with a late injection during the compression stroke to provide local enrichment around the spark plug region. All of the valve and injection timings can be found in <u>Table 1</u>. With the firing order 3-4-2-1, cylinder number 3 was set as the first one to fire and cylinder 1 the last. Since the interest of this paper is the very first firing event, which presents the strongest transient behavior, only cylinder 3 was simulated and compared with experiments, and the ignition timing for this event was 10° BTDC.

CFD Model

All the simulations in this research were carried out using CONVERGE CFD™ (CONVERGE below for short), a commercial three-dimensional CFD package widely used in engine simulations [e.g., <u>17</u>, <u>19</u>, <u>20</u>]. The modeled engine geometry is shown in Figure 1, with the piston at BDC. CONVERGE can automatically generate the grid during the runtime, which saves considerable time for the users. It will repeat the mesh generation process when the piston or the valves move, or create a finer/coarser mesh as needed in the simulation. The base grid size was set to be 4 mm for the entire domain. However, a fixed embedding was applied in the regions where finer resolution was required, such as near the valves, near the injector during fuel injection events, and in the spark plug region during the ignition period. In addition, another technique called adaptive mesh refinement (AMR) was used to further improve the mesh for the regions where the temperature or velocity was changing dramatically.

Two cycles were simulated in the runs, with the 1st one simulating the cranking cycle (without injection or ignition),

FIGURE 1 Engine geometry used in the simulation.



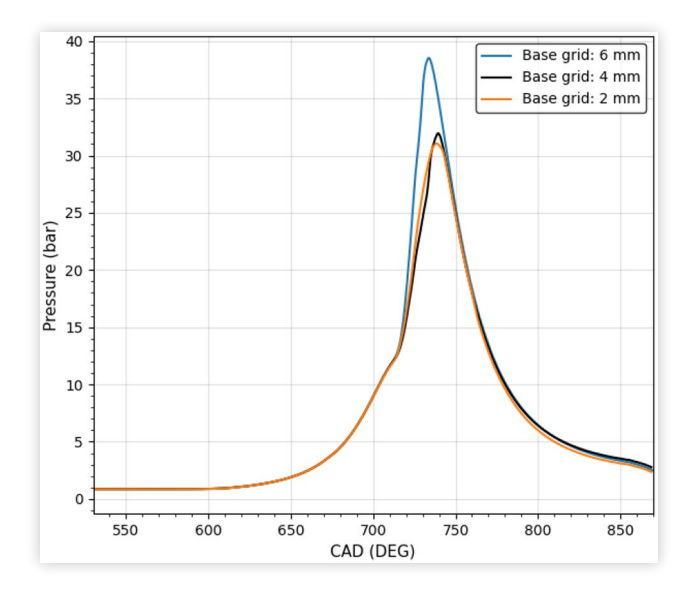
needed in the experiments for engine position synchronization, and the 2nd one simulating the first firing event of the cold start cycle. The firing cycle simulations started at 360 CAD as TDC of the intake stroke and ended at 1080 CAD as TDC of the exhaust stroke. The initial intake pressure was set as the experimental intake manifold pressure and the initial temperature was the ambient temperature. All of the wall temperatures in the engine were set the same as the ambient temperature, considering the quite short running time of the engine during the cold start process. Instead of using a fixed engine speed, a transient engine speed curve from the experiments was used in simulating the cold start process, which will be shown in detail (<u>Figure 5</u>) in the "Experimental Verification" section.

The in-cylinder air or air-fuel mixture was considered a compressible fluid. The governing equations which described the conservation of mass, momentum, and energy were solved. The transport of species was solved as well, and turbulence was modeled by the RNG k-ε model [21] of the Reynold-Averaged Navier-Stokes (RANS) method. When injected, the fuel went through a series of complicated processes until evaporated. These processes would be described using different models listed below and some key parameter settings are shown in Table 2. A Blob injection model [22] was used to set the injected drop sizes. The modified Kelvin-Helmholtz and Rayleigh-Taylor (KH-RT) models [23] were used to predict the drop breakup. For droplet collisions, No Time Counter (NTC) [24] and Post Collision Outcomes [25] methods were

TABLE 2 Parameters used in the spray models.

Models	Parameters	Values
Modified KH-RT model	KH size constant, B_0	0.6
	KH time constant, B ₁	7.0
	RT size constant, C_{RT}	0.6
	RT time constant, $C_{ au}$	1
Wall film model	Critical Weber number, We _{cric}	5.0
	Critical value for splashing, E_{cric}^2	3330
	Fraction splashed	1.0

FIGURE 2 Comparisons of cylinder pressure traces for cases with different base grid sizes: 6 mm (blue), 4 mm (black), and 2 mm (orange).



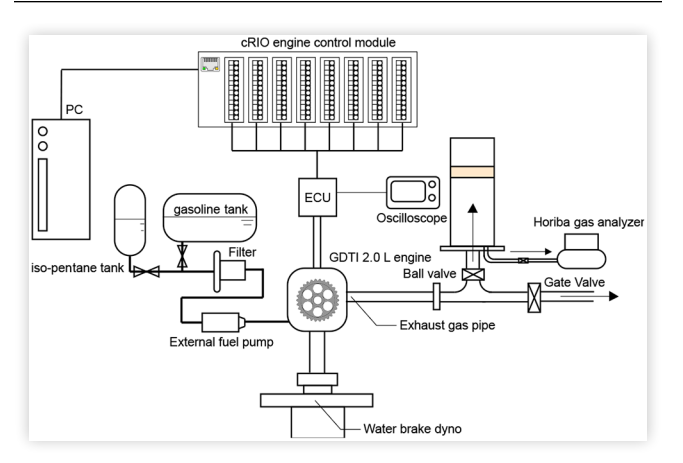
used. The effects of turbulent flow on the droplets were modeled using the O'Rourke model [26]. The wall film model was used to describe the drop-wall interactions, in which O'Rourke model [27] was used to simulate drop/film splashing. For modeling combustion of gasoline, the SAGE detailed chemical kinetics solver was used and a single component fuel, iso-octane, was used in the simulations because a detailed chemical kinetics mechanism is not available for gasoline. However, due to the importance of vapor pressure in cold start processes and because iso-octane has a much lower vapor pressure than gasoline, the vapor pressure was changed to that of gasoline having a Reid vapor pressure (RVP) of 7, with true vapor pressure (TVP) calculated from Moshfeghian's correlations [28]. The combustion chemical kinetics was modeled using the reduced i-C₈H₁₈ mechanism with 48 species and 152 reactions developed based on the paper of Liu et al. [29].

A grid independence analysis was done using three different meshes with different cell sizes. The cylinder pressure traces for cases with different base grid sizes (6 mm, 4 mm, and 2 mm) are shown in <u>Figure 2</u>. The peak pressure went down by about 6 bar when the grid size varied from 6 mm to 4 mm, but from 4 mm to 2 mm, the pressure traces were very close. So, 4 mm was chosen as the base grid size in the simulation cases discussed in the remainder of this paper.

Experimental Verification

The engine for the cold start experiments was placed in an environmental chamber with controlled ambient temperature. The ambient and coolant temperatures were kept at 22±1 °C during all of the experiments. A water brake dynamometer was coupled to the flywheel of the engine to provide a simulated idle load. The engine control unit (ECU) was replaced by a National Instruments cRIO system with custom

FIGURE 3 Schematic diagram of the cold start experiment [11].



developed programs to control the engine functions. Two different fuel tanks, filled with iso-pentane and gasoline respectively, could be switched to the fuel lines of the engine. A 4-channel oscilloscope was connected to the 4 in-cylinder pressure transducers to display the pressure traces for each cylinder. A schematic figure of the experimental setup is shown in Figure 3; more details about the experiments can be found in 2 previous papers [11, 30] of our cold start study.

A rotational incremental encoder was attached on the flywheel and its pulse signals were captured by the oscilloscope and used to calculate the high-resolution instantaneous engine speed. The engine speed curve is critical for the simulation; ten curves from different cold start experiments on different days are shown in <u>Figure 4</u>. The curves followed the same trend, although some variations could be seen. All were quite close in the range of 710 to 750 CAD, which was the period of turbulent combustion in the 1st firing event. One of these curves was arbitrarily chosen to be used in the

FIGURE 4 Transient engine speeds from 10 experimental results on different days.

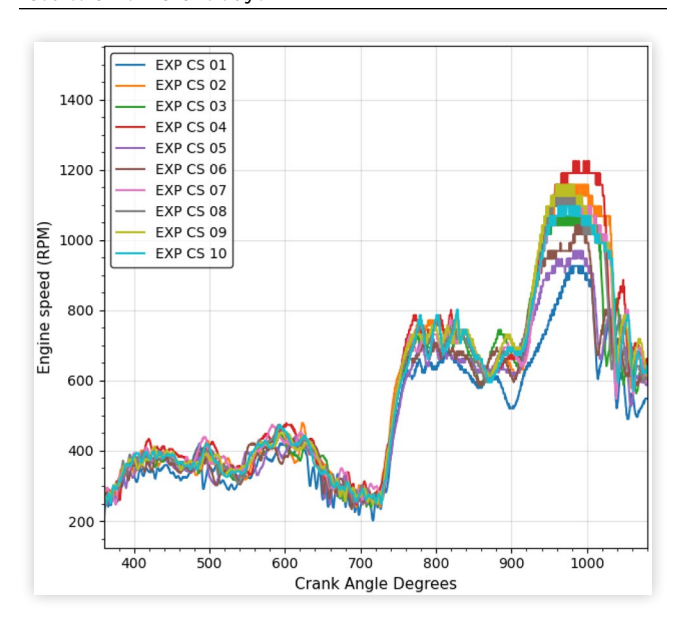
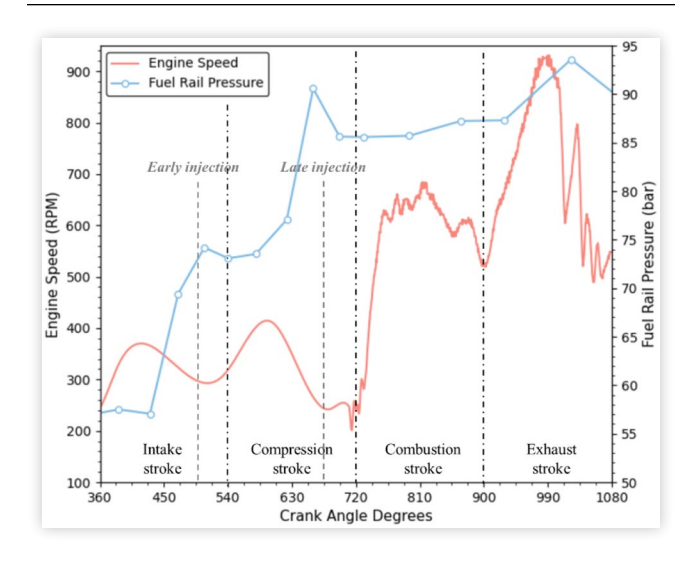


FIGURE 5 Transient engine speed (red) and fuel rail pressure (blue) curves of the first firing event used in the simulations.



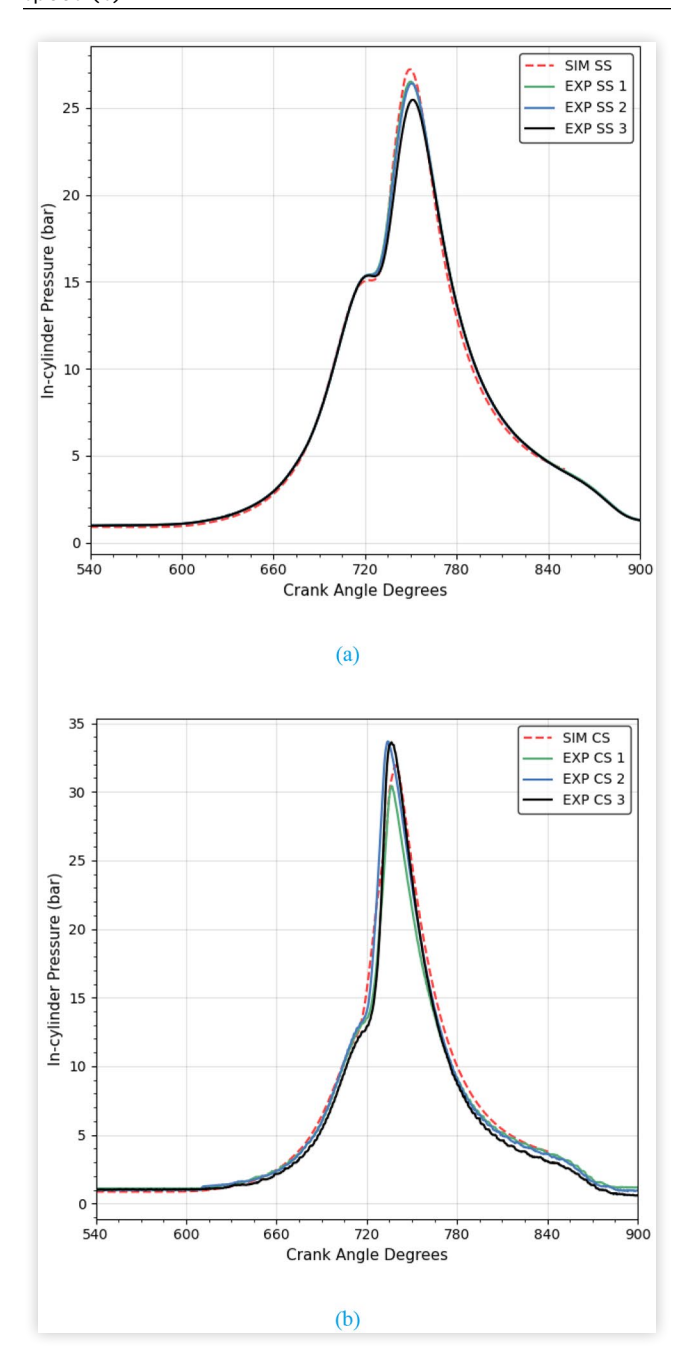
simulations after curve smoothing before ignition timing as there would be no big differences had other curves been used. Curve smoothing was applied to ignore the small oscillations probably due to tortional vibrations in the drivetrain. The transient engine speed curve used in the simulation is shown in Figure 5.

As seen in Figure 5, the engine speed remained around 300 RPM prior to combustion. The cranking speed reached a minimum of about 200 RPM right before the first firing event with an increase in pressure late in the compression stroke due to mass addition. After the ignition at 10° BTDC (710 CAD) and the following combustion process, the engine speed increased sharply to about 620 RPM within about 50 CAD, then kept slowly increasing. As combustion progressed and the exhaust valve of cylinder 3 opened (early EVO strategy), the engine speed would decrease gradually until the firing event of cylinder 4 (second cylinder to fire). A similar process repeated for the rest of the crank angle period shown in Figure 5: the engine then sped up after the 2nd cylinder's 1st firing event to above 900 RPM and slowed down as most of the fuel in cylinder 4 was burned.

Transient behavior was also characteristic for the fuel pressure as seen in Figure 5. The FRP reached 57 bar in the cranking cycle and continued to rise during the cold start, but was still quite low compared to the normal working pressure (about 160 bar), leading to poor atomization of the fuel. The instantaneous engine speed and the low FRP are very important in the simulation to capture the performance of the combustion during the cold start process, which will be shown in the following parts of the paper.

The pressure traces in the simulation were compared with the experimental results for both steady-state cases with constant engine speed and for the cold start cases with transient engine speed. The results are shown in Figure 6. Note that in the test conditions of the steady-state cases, the dual injection strategy was also used, and the ignition timing was 10° BTDC. Each steady-state experimental curve in Figure 6a

FIGURE 6 Comparisons between the simulations and experiments: steady-state cases with constant engine speed of 1765 RPM (a), and cold start cases with transient engine speed (b).



represents the averaged results of 100 continuous engine cycles. However, each cold start experimental curve in Figure 6b corresponds to only one cold start experiment after the engine had sat overnight. It is difficult to carry out multiple repetitions of cold start experiments in one day, due to the engine warming up and the residual fuel in the cylinder. So, the three cold start curves come from three different days. Overall, the pressure traces in both the steady-state and the cold start cases were quite close to the corresponding experimental curves.

Results and Discussion

Effects of Engine Speed

As shown in Figure 5, the engine speed changes with CAD during the 1st firing cycle of the cold start and the effects will be discussed in this section. Three steady state cases with different constant engine speeds (320, 700, and 1200 RPM, all the other numerical settings were the same) were simulated for comparison with the cold start case; the pressure traces are shown in Figure 7. It can be seen that the peak pressure is the highest in the transient engine speed case and the higher the RPM, the lower the peak pressure for the steady state cases. Two main reasons account for this: fuel distribution and turbulence.

Fuel Distribution The fuel distributions in the cylinder will be discussed first.

The tumble ratio is defined as the ratio of the angular speed of the flow (ω_{gas}) about the center of the mass to the angular speed of the crankshaft $(\omega_{crankshaft})$.

tumble ratio =
$$\frac{\omega_{gas}}{\omega_{crankshaft}}$$
 (1)

The tumble ratios in the combustion chamber are shown in <u>Figure 8</u>. They were very similar for the different engine speed cases before the early fuel injection event, but the induced tumble ratio changed when fuel was injected. As a result of the dual injection strategy, three sudden transitions were found, at around 510 (early fuel injection), at 670 (late fuel injection) and at 680 CAD (late fuel injection reflected by the piston bowl) in the low engine speed cases (RPM=320 and transient RPM). The changes were not so obvious in the high engine speed cases (RPM=700 and 1200).

FIGURE 7 Predicted pressure traces with different engine speeds: RPM=320 (blue), 700 (orange), 1200 (green), and transient engine speed of cold start (black).

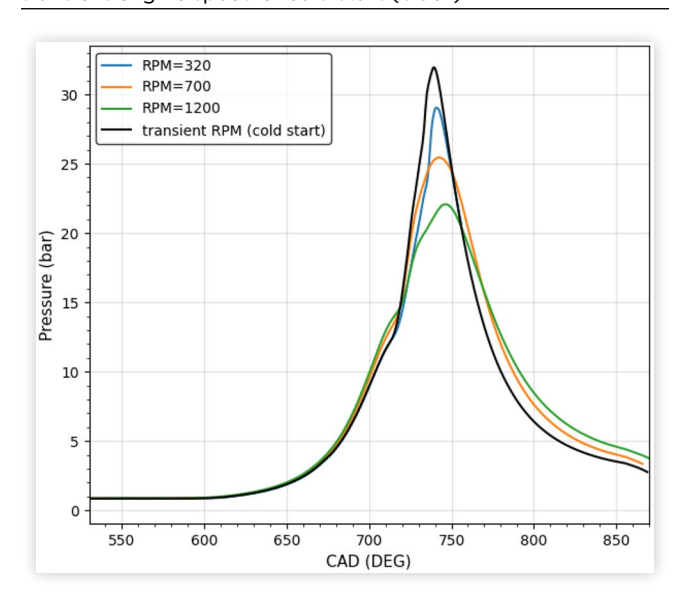
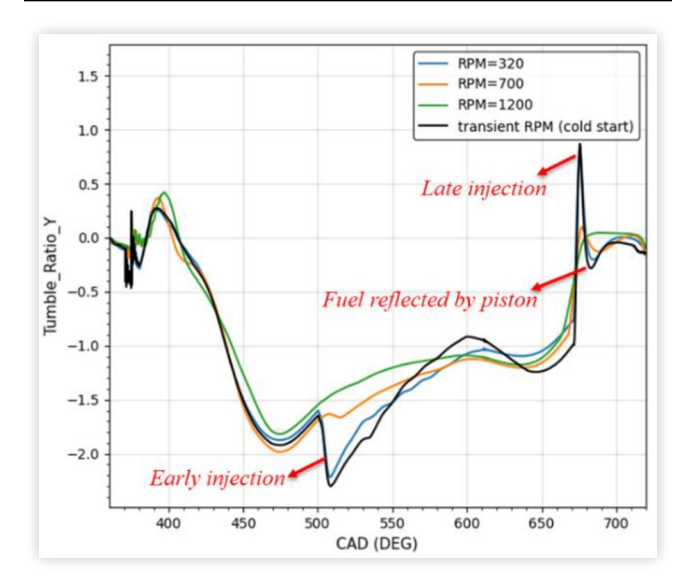


FIGURE 8 Tumble ratio in the combustion chamber as a function of engine speeds: RPM=320 (blue), 700 (orange), 1200 (green), and transient engine speed (black).



Prior to the early fuel injection event, the bulk fluid motion in the tumble direction was stronger in the high engine speed cases, consistent with the very similar tumble ratio and the high $\omega_{crankshaft}$. The same FRP, injection timings and injected fuel mass were used in the different cases, so the injection velocities were the same. The stronger fluid motion for the high engine speed cases was more "resistant" to the same injection momentum, and thus the induced tumble ratio was much higher for the low engine speed cases than the high speed cases.

Consequently, the fuel distributions at the ignition timing in the combustion chamber were different due to the different tumble ratios. The fuel distributions were mainly determined by a combination of the bulk flow advection and fuel diffusion. It is known that the turbulence intensity level (u') scales linearly with the engine speed (RPM) [31],

$$u' \propto RPM$$
 (2)

So, the diffusion rate (per crank angle) enhanced by the turbulence should be almost the same for the different engine speed cases. However, the tumble ratio in the cylinder was different, which would drive more fuel to other regions for the low engine speed cases and lead to a more uniform fuel distribution.

Next, the bulk flow and fuel motion in the combustion chamber near and after the late injection are shown in Figure 9, in which the equivalence ratio contours in the transient engine speed case are shown with the black streamlines and red arrows indicating the bulk flow direction. By 670 CAD, the early injection had established the background equivalence ratio distribution in the combustion chamber. Following that, the late fuel injection can be seen at 675 CAD. The fuel would hit the piston bowl and then would be deflected to the exhaust side, hitting the cylinder head at 680 CAD. By 680 and 685 CAD, the fuel was divided into two parts along the contours of the Y plane, with one part moving back to the intake side from the top of the combustion chamber and the other travelling further to the exhaust side. The first part would then move along two symmetric eddies on the intake side, shown in the Z plane as two lower left red arrows at 700 and 705 CAD. The second part would then separate out and move back from the periphery of the cylinder, as seen in the Z plane at 685-705

FIGURE 9 Bulk flow directions and equivalence ratio contours at different crank angles in the transient engine speed case

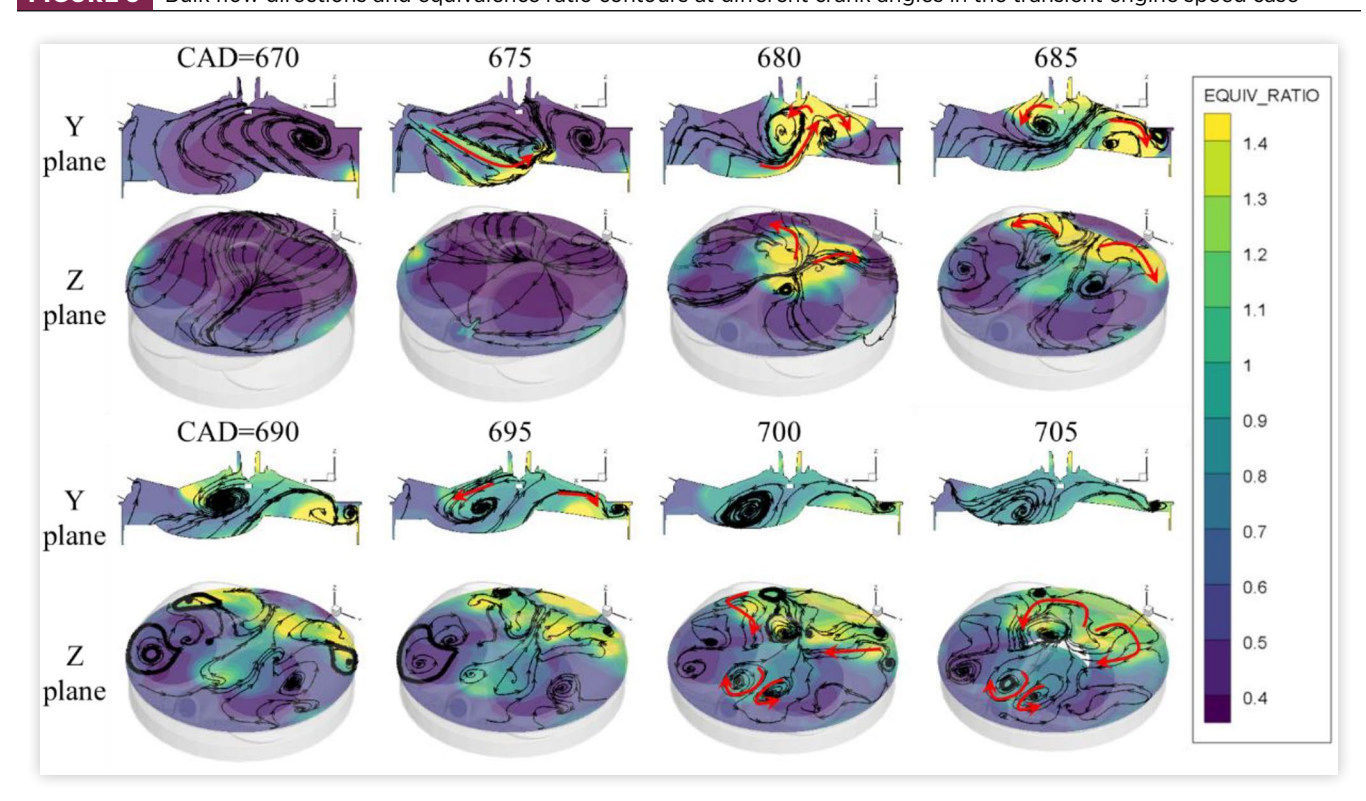
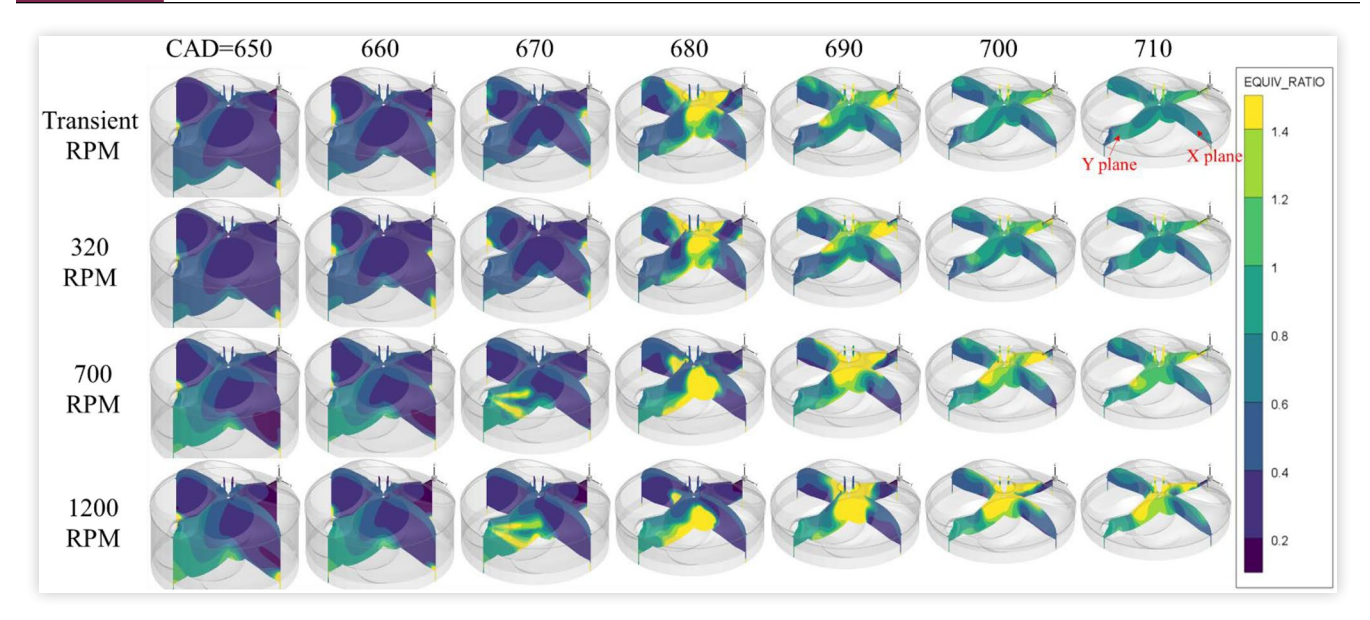


FIGURE 10 Equivalence ratio distributions at different crank angles in different engine speed cases.



CAD. This bulk motion in the combustion chamber determined the equivalence ratio distribution at the time of ignition. It should be noted that the overall bulk flows for the other engine speed cases were all very similar to what is shown in Figure 9.

The equivalence ratio distributions for different engine speed cases are compared in Figure 10, where two perpendicular cut planes (plane X and Y) through the centerline of the cylinder are shown. The end timing of the late injection was the same for the different cases, 45° BTDC as mentioned in Table 1. The FRP and injected mass were kept the same for the different cases, while the calculated injection durations in crank angles were different, based on the corresponding engine speed. That was why the fuel injection process can be seen at 670 CAD for the 700 and 1200 RPM cases, while the same process happens somewhere between 670-680 CAD for the transient RPM and 320 RPM cases. It was interesting that more fuel (rich region, yellow color) would concentrate in the center region and on the Y planes in the high engine speed cases at ignition timing (710 CAD), while the fuel is relatively more uniform for the low engine speed cases. As discussed earlier, the tumble ratio and bulk flow are the main reasons.

The average equivalence ratio (Phi_ave) and the equivalence ratio near the spark plug region (Phi_SP) are compared in <u>Table 3</u>. The average equivalence ratios were almost the same for the different cases, and all on the lean side due to the

TABLE 3 Average equivalence ratio and equivalence ratio near spark plug at ignition timing.

Cases	Average equivalence ratio (Phi_ave)	Equivalence ratio near the spark plug region (Phi_SP)
RPM=320	0.82	0.99
RPM=700	0.82	1.20
RPM=1200	0.81	1.40
Transient RPM	0.83	0.94

low evaporation rate at the low temperature. The equivalence ratios near the spark plug region were quite different; the mixture would become richer at higher engine speeds and was almost stoichiometric for the transient RPM and 320 RPM cases (the same trends could be seen in Figure 10).

To better visualize the fuel distribution for the different engine speed cases, the fuel was divided into different bins with different equivalence ratio ranges. These bins at the time of ignition are shown in Figure 11, where each individual point represents the mass fraction of the fuel falling into the specified equivalence ratio range. Most fuel fell in the range around 0.8, which was the average equivalence ratio shown in Table 3. The mass fraction in the very lean bin (below 0.5) or very rich bin (above 1.4) was higher for the high engine speed cases (700 and 1200 RPM) than for the low engine speed cases (320 and transient RPM). It is very important to know the equivalence ratio distribution, since different equivalence ratios will lead to different flame speeds, and thus different burning velocities of the fuel, different pressure traces, and different values of the indicated mean effective pressure.

FIGURE 11 Equivalence ratio distributions at ignition timing in the combustion chamber: RPM=320 (blue), 700 (orange), 1200 (green), and transient engine speed (black).

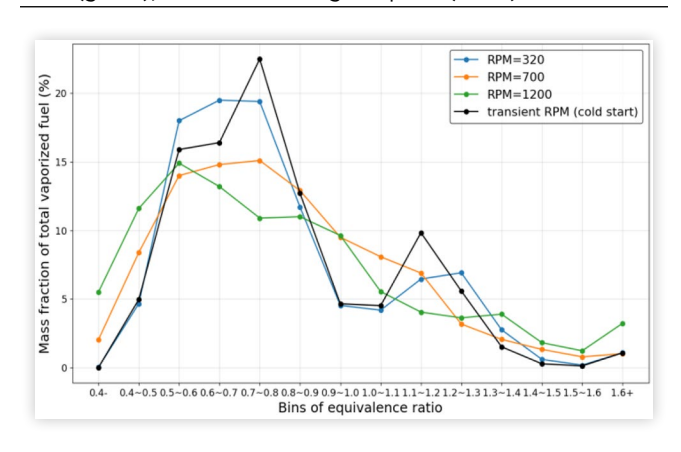
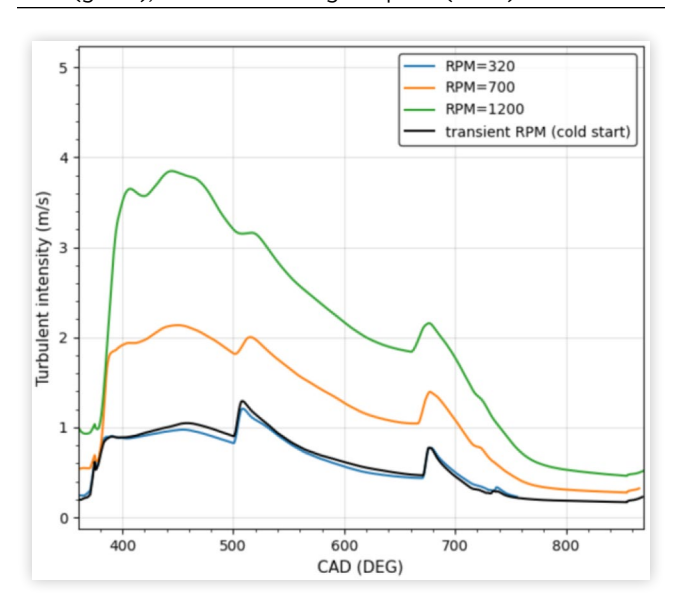


FIGURE 12 Turbulence intensity versus crank angle in different engine speed cases: RPM=320 (blue), 700 (orange), 1200 (green), and transient engine speed (black).



Turbulence As given by Eqn. (2), turbulence intensity scales approximately linearly with the engine speed. This is shown in Figure 12 as well, where the average turbulence intensity in the combustion chamber is plotted versus crank angle for the different engine speed cases. The turbulence level for the transient engine speed case was very close to the 320 RPM case, since the transient speed stayed around 320 RPM for most of the time before ignition.

Shown in [31], the burning velocity (S_b) for steady turbulent combustion conditions scales linearly with turbulence intensity. Combined with Eqn. (2), we have,

$$S_b \propto u' \propto RPM$$
 (3)

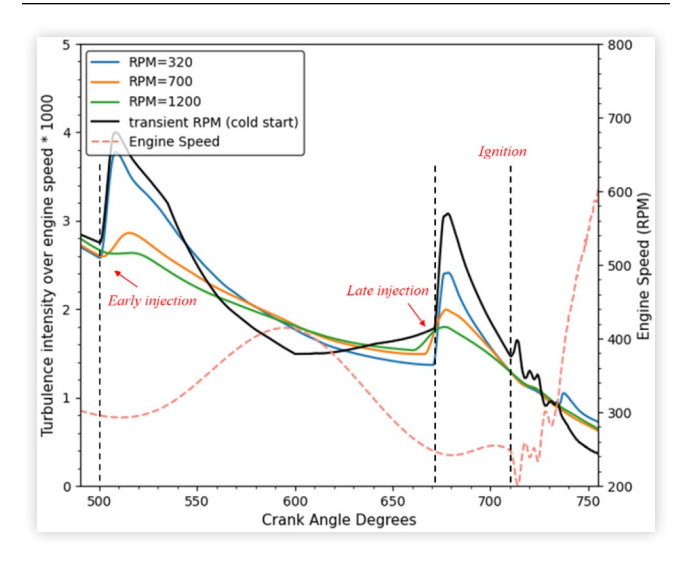
Then the mass fuel burnt (m_{burnt}) per crank angle has the relation:

$$\frac{\Delta m_{burnt}}{\Delta CAD} \propto \frac{S_b * \Delta t}{\Delta CAD} \propto u' \frac{\Delta t}{\Delta CAD} \propto \frac{u'}{RPM} \tag{4}$$

In general, <u>Eqn. (4)</u> indicates that the increased turbulence level can compensate for the reduced actual time when the engine speed increases and, thus, gives almost the same combustion pressure or the same burnt fuel mass at the same crank angles. But some different behavior was observed for the transient engine speed case.

The average turbulence intensity in the cylinder normalized by the instantaneous engine speed, and then scaled up by a factor of 1000 (to make it easier to read), i.e., 1000*u'/RPM, is plotted versus crank angle in Figure 13, with the instantaneous engine speed shown as well. The normalized turbulence levels for the three constant engine speed cases were very close, consistent with $u' \propto RPM$ (shown in Eqn. (2)), except for the crank angles after the early and late injections, where the different heights of the peaks are caused by the same injecting velocities but different engine speeds. But the injection-induced turbulence decays very rapidly with crank angle, falling to the same level at the time

FIGURE 13 Turbulence intensity over engine speed scaled up by a factor of 1000 as a function of crank angle in different engine speed cases: RPM=320 (blue), 700 (orange), 1200 (green), and transient engine speed (black, the instantaneous engine speed of this case is shown as the red dashed curve).



of ignition. For the transient engine speed case, the turbulence did not change rapidly with crank angle when the engine speed changed quickly. So, the black normalized turbulence curve had a trend opposite that of the instantaneous engine speed. It is worth noting that the normalized turbulence level in the transient engine speed case was higher than the other constant engine speed cases for about 20 degrees after ignition, which led to stronger initial combustion and thus more fuel burnt after the same crank angle, based on Eqn. (4).

Overall Effects To summarize the effects of both fuel distribution and turbulence on the combustion, the mass fraction burnt (MFB) curves are shown in <u>Figure 14</u>, where the horizontal axis is time, with the unit of seconds, in <u>Figure 14a</u> and crank angle degrees in <u>Figure 14b</u>. The zero point of <u>Figure 14a</u> corresponds to the ignition timing, 710 CAD.

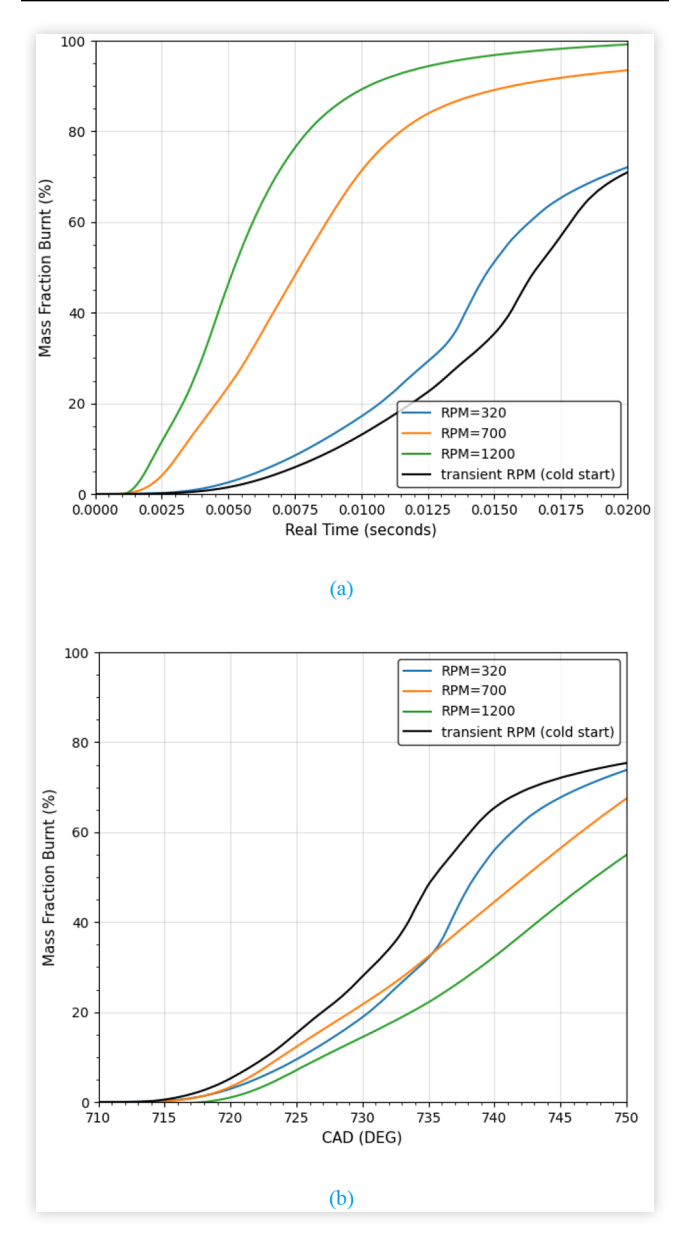
Here MFB is defined as the fuel mass burnt (m_{burnt}) divided by the total evaporated fuel $(m_{evaporated})$ at the corresponding time:

$$MFB = \frac{m_{burnt}}{m_{evaporated}} \tag{5}$$

The fuel was burned very quickly with respect to time for the high engine speed cases (<u>Figure 14a</u>), mainly due to the high levels of turbulence shown in <u>Figure 12</u>. Again, the MFB vs. time curve for the transient RPM was close to the 320 RPM case, due to their similar engine speeds.

Instead of the absolute turbulence level shown in Figure 12, the RPM-normalized turbulence intensity in Figure 13 should be considered when comparing the MFB vs. CAD curves. The three constant engine speed cases shared a similar normalized turbulence level after ignition, while the equivalence ratio differences were responsible for the different burning velocities. It is known that the laminar flame speed

FIGURE 14 Mass fraction burned versus real time (a) and versus crank angle (b): RPM=320 (blue), 700 (orange), 1200 (green), and transient engine speed (black).



is the highest when the fuel air mixture is slightly rich, or the equivalence ratio is about 1.1-1.2 [29]. Since each was accelerated by the same normalized turbulence, the initial burning velocity was the highest for the 700 RPM case, was in-between for the 320 RPM case, and lowest for the 1200 RPM case (the equivalence ratio in the spark plug region was 1.20, 0.99, and 1.40 respectively, shown in Table 3). But, as the flame propagated to other regions in the combustion chamber, where the mixture inhomogeneities resulted in very lean or very rich regions in the higher speed cases (Figure 11), the MFB vs. CAD curve for 700 RPM, for example, was surpassed by the 320 RPM case after 735 CAD. The fuel distribution in the transient engine speed case was similar to the 320 RPM case, but the higher normalized turbulence strengthened the combustion and thus the MFB vs. CAD was greater than all

of the other cases. The trends in the MFB vs. CAD curve are also consistent with the pressure traces shown in <u>Figure 7</u>.

As shown in this section, both the equivalence ratio distribution and the turbulence level will be important to simulate the complicated turbulent combustion process. To capture all the details of a cold start process of an engine, a temporal or transient engine speed is highly recommended.

Effects of Vapor Pressure

Fuel vapor pressure is quite important for the cold start process to ensure enough evaporated fuel exists in the combustion chamber and that an appropriate fuel/air ratio exists for the combustion process. Three different vapor pressures (shown in Figure 15) were examined, including low vapor pressure (iso-octane vapor pressure), gasoline vapor pressure, and high vapor pressure (iso-pentane vapor pressure), while all of the other settings in the simulations were the same.

The fuel tracking for the gasoline cold start process with the transient engine speed is shown in Figure 16, where the y axis represents the fuel mass normalized by the total injected mass. All the solid curves in Figure 16 should add up to 100% at any crank angle, which means all the injected fuel was covered. The red dash shows the total evaporated fuel in the cylinder, which was the sum of the reacted portion (green) and the unreacted gaseous portion (orange).

About 9.6% of the fuel, all from the early injection, flowed back into the intake ports before IVC, and escaped the 1st firing event. The fuel droplets of the injecting spray evaporated quite quickly, within about 10~15 crank angle degrees. Almost all the unevaporated fuel in the cylinder existed as wall films. They would start to evaporate faster after around 730-740 CAD, which was about the peak pressure location, indicating the flame started to interact with the boundary layer, causing

FIGURE 15 Vapor pressures used in the simulations: low vapor pressure (blue), gasoline vapor pressure (orange), and high vapor pressure (green).

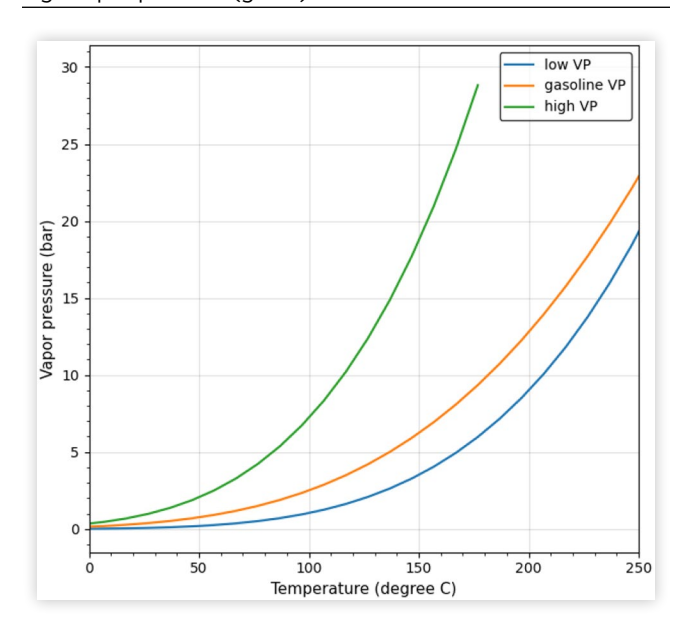
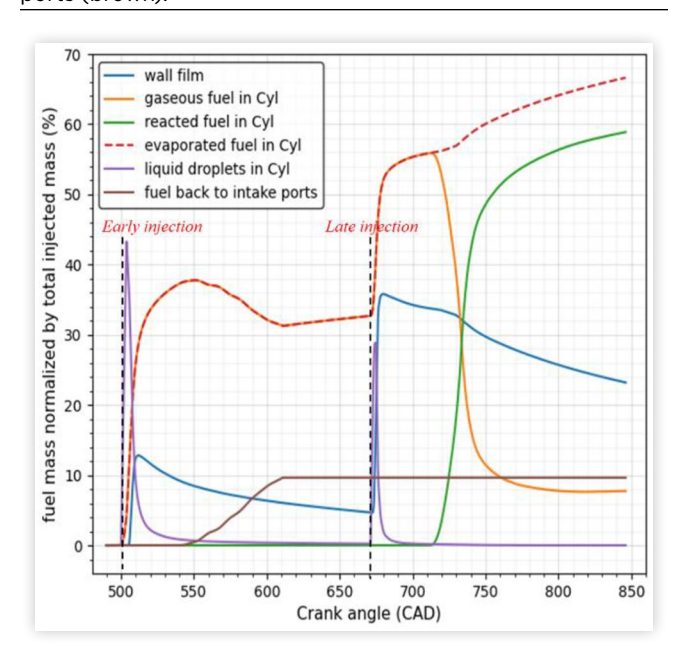


FIGURE 16 Fuel tracking for the gasoline cold start process: wall films (blue), gaseous fuel in the cylinder (orange), the fuel which has been reacted (green), total evaporated fuel in the cylinder (red dash), liquid fuel droplets in the cylinder (purple), and the fuel which flows back into the intake ports (brown).



a high near-film temperature, accelerating the evaporation process. Still about 30% of the total injected fuel remained unreacted at a very late crank angle, in which about 22% was in the liquid phase as the wall films and 8% remained unreacted in the gas phase. It should be kept in mind that the simulation did not account for fuel loss into the crankcase or that absorbed by the oil or by deposits, possible sinks in an actual engine.

The fuel distribution at the time of ignition for the three different vapor pressure cases is shown in Figure 17, where the y axis is the fuel mass normalized by the total injected fuel. As vapor pressure increased, more fuel evaporated and stayed in the gas phase, resulting in reduced wall films. The fuel which flowed back into the intake ports increased with vapor pressure as well.

The average equivalence ratios at the time of ignition for the low, gasoline, and high vapor pressure cases were 0.50, 0.94, and 1.19, respectively. This led to very strong combustion for the high vapor pressure case, and a misfire for the low vapor pressure case, which is easily seen from the pressure traces, shown in Figure 18.

Effects of Fuel Rail Pressure

Different FRPs lead to different injection durations and different injection velocities for the same amount of injected fuel. To study these effects, three cases were simulated with different FRPs, including baseline (89 bar), high FRP (119 bar), and low FRP (59 bar). The discharge coefficient remained constant in these cases, and the injection duration varied with different FRPs to keep the same amount of injected fuel.

FIGURE 17 Fuel tracking (mass fraction) at ignition timing for different vapor pressure cases: wall films (blue), gaseous fuel in the cylinder(orange), liquid droplets in the cylinder (grey) and fuel back to the intake ports before IVC (yellow).

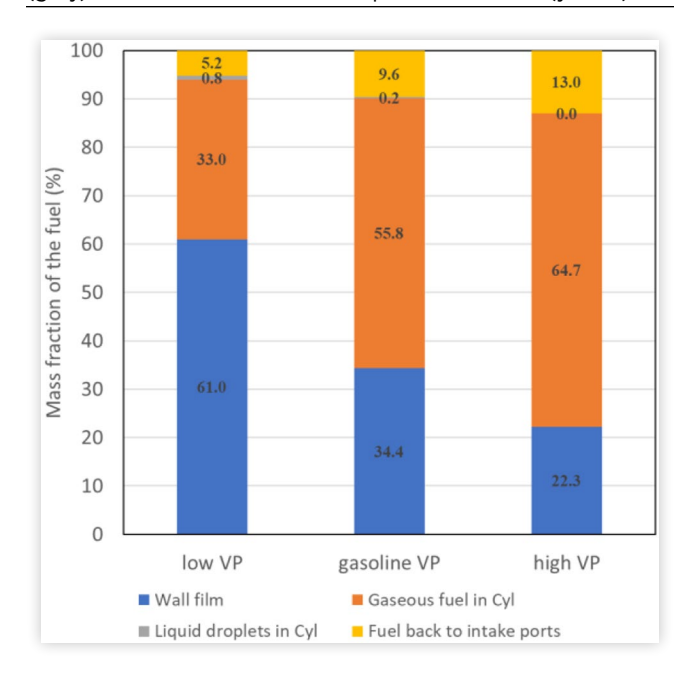
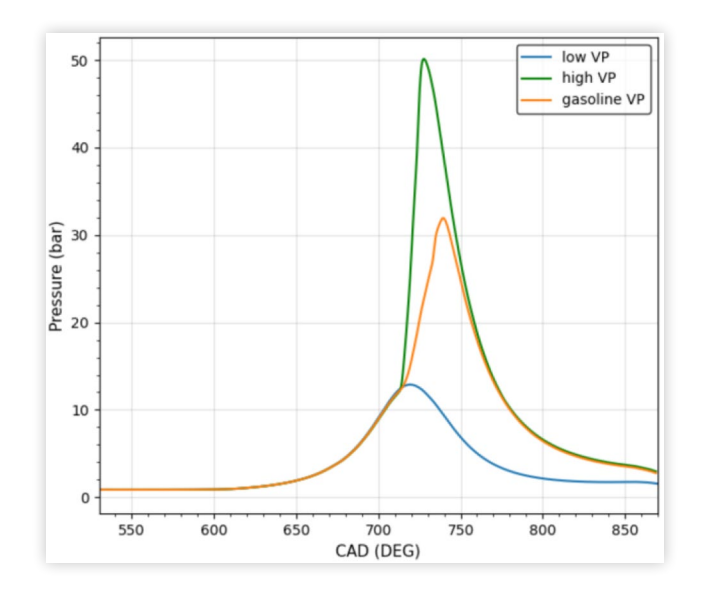
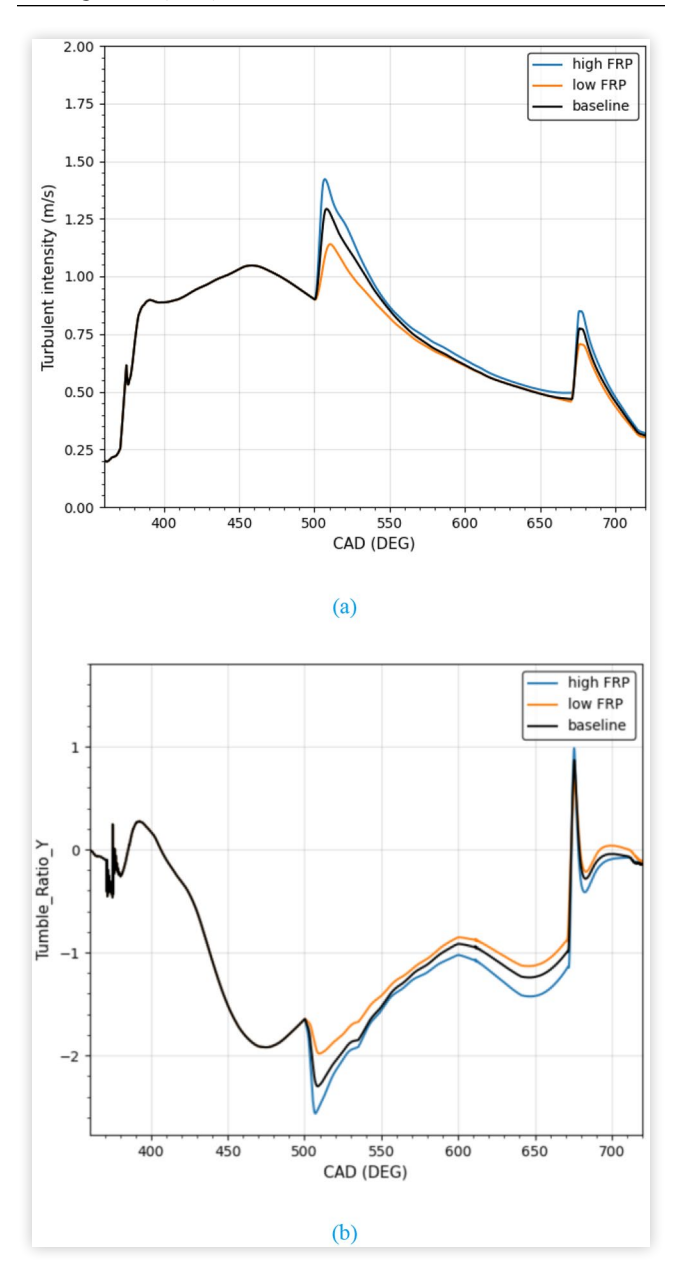


FIGURE 18 Pressure traces in the combustion chamber for different vapor pressure cases: low vapor pressure (blue), gasoline vapor pressure (orange), and high vapor pressure (green).



The turbulence intensity and tumble ratio are shown first in Figure 19, where the induced turbulence and induced tumble ratio can be found after both early and late injections. Similar results were observed in the engine speed section that the induced turbulence would decay very fast and fell to the same level around the time of ignition, so no marked effects of turbulence were expected for the combustion intensity for the different FRP cases. However, due to different injection velocities and different tumble ratios, the fuel distributions

FIGURE 19 Turbulence level (a) and tumble ratio (b) in different FRP cases: low FRP (orange), baseline FRP (black), and high FRP (blue).



in the combustion chamber are different, causing different burning velocities in each case.

To show the different fuel distributions, the equivalence ratio contours for different cases in a Z cut plane at the time of ignition are shown in <u>Figure 20</u>, where the intake side is on the left and exhaust side on the right in each image. The fuel was more homogeneous in the high FRP case, while it was richer on the exhaust side and leaner on the intake side for the low FRP case.

The average equivalence ratios for the high, baseline and low FRP cases were 0.80, 0.83, and 0.88, respectively, shown in Figure 21 together with the fuel tracking in different FRP cases. It was surprising that the higher the FRP, the more fuel was retained in the surface films and less in the gas phase. In

FIGURE 20 Equivalence ratio distribution in the cylinder at ignition timing: high FRP (left), baseline FRP (middle), and low FRP (right).

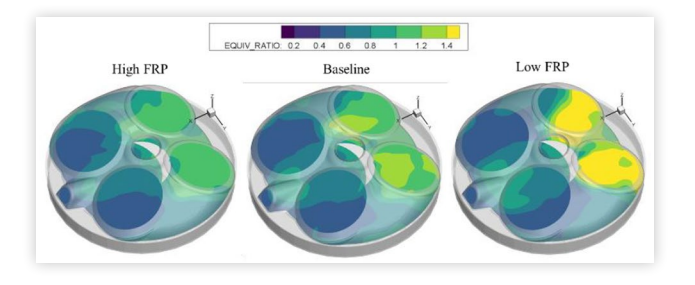
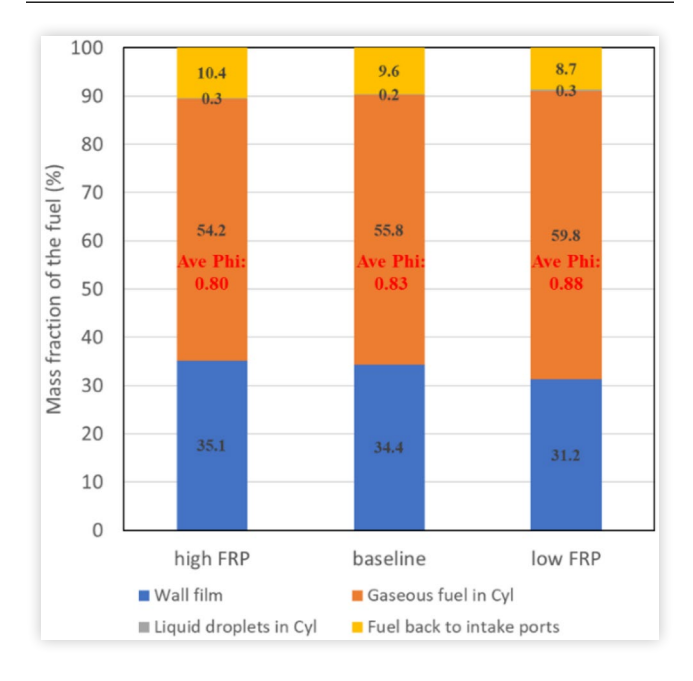


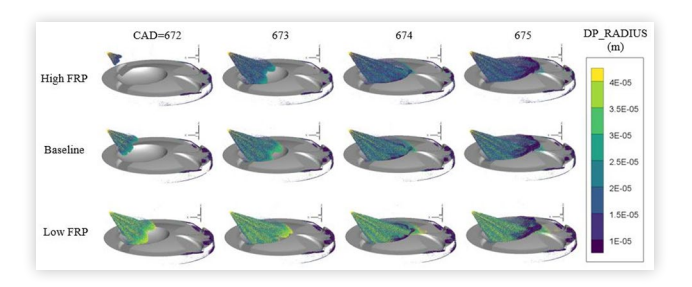
FIGURE 21 Average equivalence ratio and fuel tracking in cylinder for different FRP cases: high FRP (left), baseline FRP (middle), and low FRP (right).



general, higher FRP results in better atomization and evaporation, so a higher average equivalence ratio would be expected. For the case of cold start, however, the fuel evaporation rate from the wall films is much lower than for steady state operation due to the low surface temperatures, so the droplet-wall interaction of the fuel has to be taken into account, deviating from what might normally be expected.

Different outcomes can result when fuel droplets collide with the wall. The droplets may form a film on the wall or merge with an existing liquid film and then evaporate by absorbing heat from the wall or the surrounding gas. Drops may also rebound off a wall surface or splash into several smaller droplets off a wall, which become easier to evaporate. Both the rebound and splash portion off the wall can help reduce the film mass and increase the average equivalence ratio in the cylinder. The differences in droplet radii for each of the different cases, as visualized in Figure 22, can help understand the drop behavior after the late injection. Droplets were smaller in high FRP cases, indicating the high FRP did lead to better atomization. The fuel droplets hit the piston

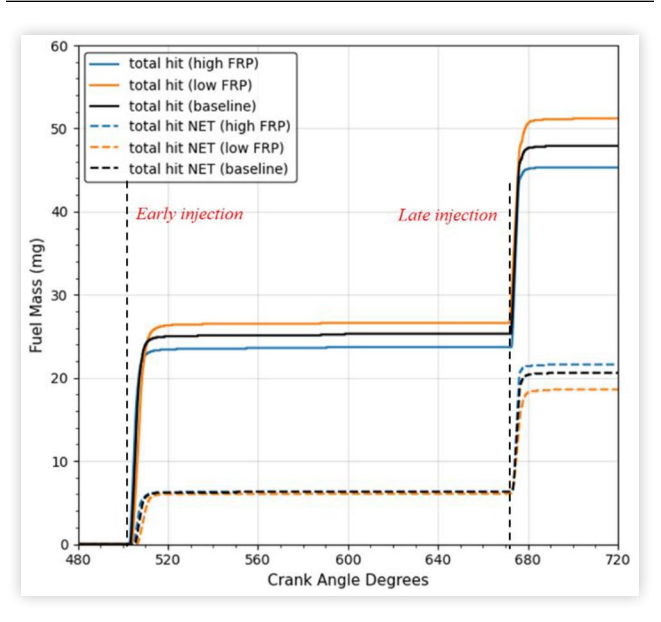
FIGURE 22 Droplet radii at different CADs in different FRP cases: high FRP (top), baseline FRP (middle), and low FRP (bottom).



bowl at 674~675 CAD, and the smaller droplets, after splashing off the piston bowl, were also captured by the simulation.

The results of the drop-wall interaction for different FRP cases are shown in Figure 23, where "total hit" refers to all of the droplets that hit or have ever hit the walls, shown as solid lines, and "total hit NET" refers to the droplets that remain on the walls after colliding with the cylinder or piston, shown as dashed lines. The difference between these two series of curves is the rebound and splash portion. After the early injection, the total hit curve for the high FRP case was the lowest, indicating more fuel evaporated directly before hitting the walls due to better atomization. However, the total hit NET curves after the early injection were very close for the three cases, meaning less fuel rebounded and splashed off the wall in the high FRP case. The trends became even more obvious after the late injection, showing that the total hit NET curve of the high FRP case was the highest of the three. Because of less fuel rebound and splashing, thicker fuel films and less gaseous fuel were obtained in the high FRP case, as shown in Figure 21.

FIGURE 23 Total hit (solid lines, all the fuel droplets which hit or ever hit the walls) and total hit NET (dashed lines, the fuel droplets which hit and remain on the walls): high FRP (blue), baseline FRP (black), and low FRP (orange).



The empirical analysis of the drop-wall interaction based on the model used in the current CONVERGE simulation was carried out as well. Drops with Weber numbers below a critical value may rebound off a surface, as shown in <u>Eqn. (6)</u>.

$$We_i = \frac{\rho_l V_n^2 d}{\sigma} < We_{cric} \tag{6}$$

where ρ_l is the liquid fuel density, V_n is the drop velocity component normal to the wall, d is the diameter of the drop, and σ is the liquid fuel surface tension.

The O'Rourke model $[\underline{27}]$ is used to simulate fuel splash, where the criterion for splash is given as $\underline{Eqn. (7)}$.

$$E_i^2 = \frac{We_i}{\min\left(\frac{h_\alpha}{d}, 1\right) + \frac{\delta_{bl}}{d}} > E_{cric}^2$$
 (7)

where 3330 is used as E_{cric}^2 as suggested by O'Rourke and Amsden [27], $h\alpha$ is the local film thickness, d is the diameter of the drop and δ_{bl} is the boundary layer thickness, given by:

$$\delta_{bl} = \sqrt{\frac{\mu_l d}{\rho_l V_n}} \tag{8}$$

where μ_l is the liquid fuel viscosity.

To compare the relative possibility of rebound and splash after the late injections in different cases, the average droplet velocity and Sauter mean diameter (SMD) near the piston bowl were used in Eqn. (6) and (7), and 45° was used to calculate the normal velocity component for simplicity. Considering that different droplets might have different injection velocities, diameters and incident angles, the calculated results utilizing the average values, shown in Eqn. (9) and (10), were only an estimation for the average droplet-wall behavior.

$$We_{i(hioh)}: We_{i(haseline)}: We_{i(low)} = 1.11:1:0.87$$
 (9)

$$E_{i(high)}^{2}: E_{i(baseline)}^{2}: E_{i(low)}^{2} = 0.93:1:1.13$$
 (10)

In the high FRP case, the calculated average We_i was higher and E_i^2 was lower, indicating the fuel would be more unlikely to rebound or splash when FRP was increased, at least within the covered pressure range.

The summary of FRP effects on combustion is shown in Table 4. Although different turbulence levels were induced in different cases due to different injection velocities, it decayed to the same level around the time of ignition. Both the average equivalence ratio and the fuel distribution changed with FRP, leading to different combustion intensities. The higher the FRP, the more homogeneous the fuel distribution would be, but less fuel would evaporate. Finally, the overall effects were indicated by the cylinder pressure traces, shown in Figure 24. The curves overlapped over most of the crank angle range, and the peak pressure differences were within approximately 20%. Nevertheless, inferred from the figure, the baseline would give the best performance of the three.

Three experimental results are shown for comparison with the simulation for the low FRP in <u>Figure 25</u>, where each solid curve represents one individual experimental pressure trace. The FRP used in all these three experiments was 65 bar, 6 bar higher than the value (59 bar) used in the simulation for the low FRP case, but the resulting differences should not

TABLE 4 Summary of the FRP effects on combustion.

Case	Turbulence	Equivalence ratio Distribution	Average Equivalence Ratio	Overall Performance
Low FRP	Ave	Bad	Good	Ave
Baseline	Ave	Ave	Ave	Good
High FRP	Ave	Good	Bad	Bad

FIGURE 24 Pressure traces in the combustion chamber for different FRP cases: high FRP (blue), baseline FRP (black), and low FRP (orange).

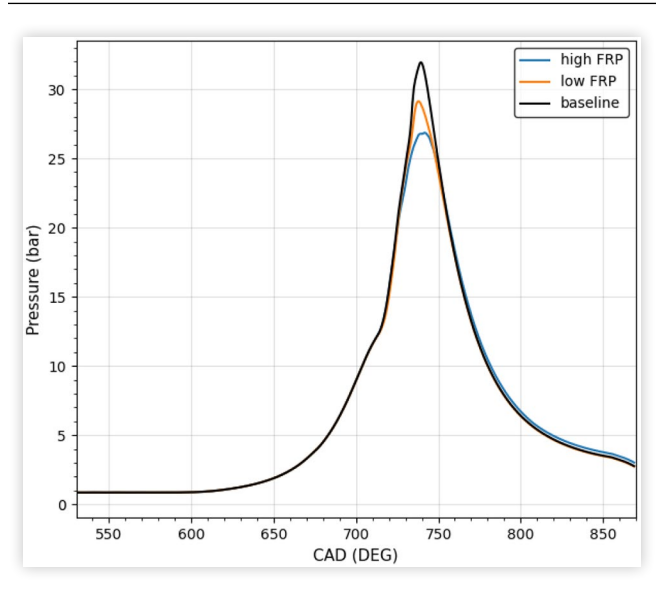
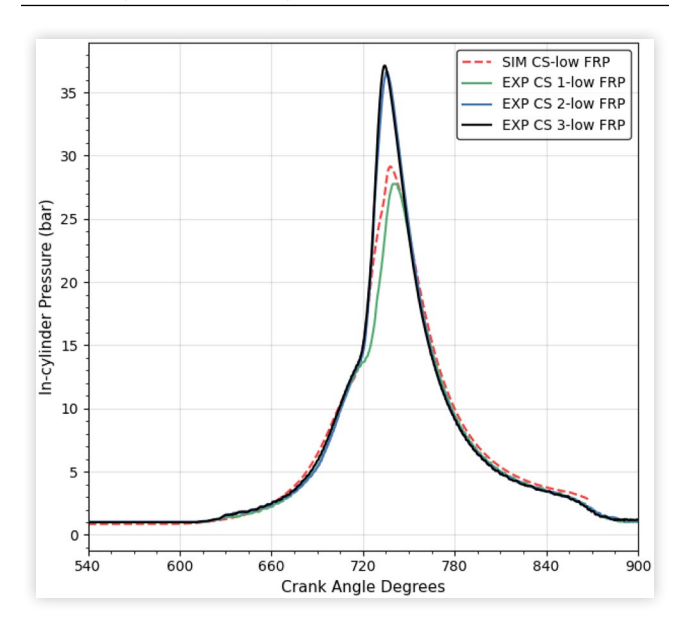


FIGURE 25 Comparisons of pressure traces between the simulations and experiments: simulation results for low FRP at 59 bar (red dashed line) and experimental results for low FRP at 65 bar (three solid lines).



be very sensitive to the difference. Variations were observed for the three experimental pressure traces. The simulation curve followed the same trend and was between the three experimental ones. Compared with the baseline experimental pressure traces shown in <u>Figure 6b</u>, the peak pressure, for both baseline and these three low FRP experiments, ranged from about 30 to 35 bar, so it was hard to tell which FRP was better, based solely on the pressure curves.

It should be noted that the droplet-wall interaction was considered based on the wall film model in CONVERGE in this work. There are other models to describe the interactions as well, where drop behavior is defined based on different criteria. Besides, turbulence varies in a more chaotic way in a real engine, making the droplet behavior even more difficult to predict and leading to cycle-to-cycle variations (as shown in Figure 25). So, there should be an optimal FRP value, but it was difficult to determine. Overall, the results suggest that droplet-wall interactions are important when considering the effect of FRP and merit careful consideration in studies of the cold start process in engines.

Summary and Conclusions

CFD modeling using CONVERGE was applied to the 1st firing event of the engine cold start process. Different engine parameters, including transient engine speed, fuel vapor pressure, and fuel rail pressure, were studied to show how they affected the in-cylinder mixture distribution, the turbulence level, and the combustion intensity. Fuel tracking was performed to help understand the fuel behavior after injection. The transient engine speed and the fuel rail pressure used in the simulations came from the companion experiments.

The primary conclusions from this study were:

- 1. The fuel from the late (2nd) injection hit the piston bowl first, and was then deflected to the exhaust side, hitting the cylinder head. Finally, the fuel was advected back from the exhaust side to the intake side.
- The in-cylinder air fuel mixture at the time of ignition was more homogenous for the low engine speed case due to a strong tumble flow induced by the late injection, while more fuel stayed in the very rich and lean regions for the high engine speed case.
- 3. The RPM-normalized turbulence levels for the constant engine speed cases were approximately independent of engine speed, except for the crank angles immediately following the early and late injections. The injection-induced turbulence intensity fell to the same level by the time of ignition, however. For the transient engine speed case, the turbulence did not change rapidly with crank angle when the engine speed changed quickly. Due to a low engine speed early in the transient, the normalized

- turbulence was higher than for the constant engine speed cases for about 20 crank angle degrees after the ignition event.
- 4. The spark plug region equivalence ratio at the time of ignition for the 700 RPM case, 1.20, led to the strongest initial combustion of the three simulated constant engine speed cases. But due to the mixture inhomogeneities in the combustion chamber, the pressure trace was surpassed later by the 320 RPM case. The MFB vs. CAD curve in the 1200 RPM case was the most retarded due to the very rich fuel mixture near the spark plug at the time of ignition. Due to a more homogeneous mixture distribution and the higher normalized turbulence level in the cylinder, the MFB vs. CAD curve for the transient engine speed case was the most advanced of the cases.
- 5. Fuel tracking for the gasoline vapor pressure case showed that about 9.6% of the fuel flowed back into the intake ports before IVC; still 22% of the total injected fuel remained as liquid films on the walls at a very late crank angle and 8% remained unreacted in the gas phase.
- As expected, more fuel evaporated, and thus higher combustion pressures were achieved as fuel vapor pressure increased.
- 7. For the different FRP cases, the turbulence levels were very close at the time of ignition, but the high FRP helped establish a more homogeneous fuel distribution.
- 8. High FRP contributed to more evaporated fuel before the fuel hitting the wall surfaces. However, the splash and rebound fuel fraction off the walls was even less, leading to less total gaseous fuel and a lower average equivalence ratio.
- Considering the combined effects of turbulence, fuel distribution and average equivalence ratio, the baseline FRP case presented the best performance of combustion, though the cylinder pressure difference was not huge.

In summary, the transient conditions are very important to consider in the engine cold start process, and yield results that are different from the steady state cases. Both the engine speed and the FRP can affect the fuel mixture distribution in the cylinder and lead to different burning velocities. The transient engine speed, especially the low engine speed around the time of ignition, allows more time for flame propagation near TDC, resulting in higher peak pressures. This result in the simulations was through the higher RPM-normalized turbulence level for the initial combustion. In addition, unlike the steady state case, the liquid film evaporation process is very slow during first cold start firing event due to the low wall temperature. That is why the appropriate fuel vapor pressure has to be used and the droplet-wall interactions deserve thorough consideration.

References

- 1. Zhao, F., Lai, M.-C., and Harrington, D.L., "Automotive Spark-ignited Direct-injection Gasoline Engines," *Progress in Energy and Combustion Science* 25, no. 5 (1999): 437-562, doi:10.1016/S0360-1285(99)00004-0.
- Rotondi, R. and Bella, G., "Gasoline Direct Injection Spray Simulation," *International Journal of Thermal Sciences* 45, no. 2 (2006): 168-179, doi:10.1016/j.ijthermalsci.2005.06.001.
- 3. Deng, Y., Feng, C., Jiaqiang, E., Wei, K. et al., "Performance Enhancement of the Gasoline Engine Hydrocarbon Catchers for Reducing Hydrocarbon Emission during the Cold-start Period," *Energy* 183 (2019): 869-879, doi:10.1016/j.energy.2019.06.183.
- 4. Eng, J.A., "The Effect of Spark Retard on Engine-out Hydrocarbon Emissions," SAE Technical Paper 2005-01-3867 (2005). https://doi.org/10.4271/2005-01-3867.
- Burke, D., Foti, D., Haller, J., and Fedor, W.J., "Fuel Rail Pressure Rise during Cold Start of a Gasoline Direct Injection Engine," SAE Technical Paper <u>2012-01-0393</u> (2012). https://doi.org/10.4271/2012-01-0393.
- Hoffmann, G., Befrui, B., Berndorfer, A., Piock, W.F. et al., "Fuel System Pressure Increase for Enhanced Performance of GDi Multi-Hole Injection Systems," SAE Int. J. Engines 7, no. 1 (2014): 519-527. https://doi.org/10.4271/2014-01-1209.
- Gao, J., Tian, G., Sorniotti, A., Karci, A.E. et al., "Review of Thermal Management of Catalytic Converters to Decrease Engine Emissions during Cold Start and Warm Up," *Applied Thermal Engineering* 147 (2019): 177-187, doi:10.1016/j. applthermaleng.2018.10.037.
- Han, D., Jiaqiang, E., Deng, Y., Chen, J. et al., "A Review of Studies Using Hydrocarbon Adsorption Material for Reducing Hydrocarbon Emissions from Cold Start of Gasoline Engine," *Renewable and Sustainable Energy* Reviews 135 (2021): 110079, doi:10.1016/j.rser.2020.110079.
- 9. Bäroth, T., Drochner, A., Vogel, H., and Votsmeier, M., "Effect of Diverse Hydrocarbons on the Cold Start Behavior of Three-Way Catalysts," *Top Catal* 60, no. 3-5 (2017): 278-282, doi:10.1007/s11244-016-0609-8.
- 10. Yan, X., Sone, R., Inoue, R., Kusaka, J. et al., "Modeling Three-Way Catalyst Converters During Cold Starts And Potential Improvements," SAE Technical Paper 2019-01-2326 (2019). https://doi.org/10.4271/2019-01-2326.
- Hu, J., Hall, M., Matthews, R., Moilanen, P. et al., "Quantitative Analysis of Gasoline Direct Injection Engine Emissions for the First 5 Firing Cycles of Cold Start," SAE Technical Paper 2021-01-0536 (2021). https://doi. org/10.4271/2021-01-0536.
- 12. Rodriguez, J.F. and Cheng, W.K., "Cycle-by-Cycle Analysis of Cold Crank-Start in a GDI Engine," *SAE Int. J. Engines* 9, no. 2 (2016): 1210-1219. https://doi.org/10.4271/2016-01-0824.
- Yamada, T., Gardner, D.V., Bruno, B.A., Zello, J.V. et al., "The Effects of Engine Speed and Injection Pressure Transients on Gasoline Direct Injection Engine Cold Start," SAE Technical Paper 2002-01-2745 (2002). https://doi.org/10.4271/2002-01-2745.

- 14. Titus, F., Berlet, P., Sobek, F., and Wessling, J., "Emission Reduction during Cold Start by Combustion Controlled Increase of In-Cylinder Temperatures," SAE Technical Paper 2018-01-1740 (2018). https://doi.org/10.4271/2018-01-1740.
- 15. Xu, Z., Yi, J., Wooldridge, S., Reiche, D. et al., "Modeling the Cold Start of the Ford 3.5L V6 EcoBoost Engine," *SAE International Journal of Engines* 2, no. 1 (2009): 1367-1387.
- Malaguti, S., Fontanesi, S., and Severi, E., "Numerical Analysis of GDI Engine Cold-Start at Low Ambient Temperatures," SAE Technical Paper <u>2010-01-2123</u> (2010). https://doi.org/10.4271/2010-01-2123.
- Ravindran, A.C., Kokjohn, S.L., and Petersen, B., "Improving Computational Fluid Dynamics Modeling of Direct Injection Spark Ignition Cold-start," *International Journal of Engine Research* (2020): 146808742096398, doi:10.1177/1468087420963982.
- Kim, S.-J., Hyun, S., and Park, J., "Optimization of Cold Start Operating Conditions in a Stoichiometric GDI Engine with Wall-guided Piston using CFD Analysis," SAE Technical Paper 2013-01-2650 (2013). https://doi.org/10.4271/2013-01-2650.
- 19. Jose, J., Parsi, A., Shridhara, S., Mittal, M. et al., "Effect of Fuel Injection Timing on the Mixture Preparation in a Small Gasoline Direct-Injection Engine," SAE Technical Paper 2018-32-0014 (2018). https://doi.org/10.4271/2018-32-0014.
- Ju, K., "Numerical Study on Premixed Charge Compression Ignition (PCCI) Combustion for Down-Sized Diesel Engine Using Converge," SAE Technical Paper <u>2020-32-2308</u> (2020). https://doi.org/10.4271/2020-32-2308.
- HAN, Z. and REITZ, R.D., "Turbulence Modeling of Internal Combustion Engines Using RNG κ-ε Models," Combustion Science and Technology 106(4-6):267-295, 1995, doi:10.1080/00102209508907782.
- 22. Reitz, R.D. and Diwakar, R., "Structure of High-Pressure Fuel Sprays," *SAE Transactions* 96 (1987): 492-509.
- 23. Beale, J.C. and Reitz, R.D., "Modeling Spary Atomization with the Kelvin-Helmholtz/Rayleigh-Taylor Hybrid Model," *AAS* 9, no. 6 (1999), doi:10.1615/AtomizSpr.v9.i6.40.
- 24. Schmidt, D.P. and Rutland, C.J., "A New Droplet Collision Algorithm," *Journal of Computational Physics* 164, no. 1 (2000): 62-80, doi:10.1006/jcph.2000.6568.
- 25. Post, S.L. and Abraham, J., "Modeling the Outcome of Dropdrop Collisions in Diesel Sprays," *International Journal of Multiphase Flow* 28, no. 6 (2002): 997-1019, doi:10.1016/S0301-9322(02)00007-1.
- O'Rourke, P.J., "Collective Drop Effects on Vaporizing Liquid Sprays," PhD Thesis, Princeton University, 1981.
- O'Rourke, P.J. and Amsden, A.A., "A Spray/Wall Interaction Submodel for the KIVA-3 Wall Film Model," SAE Technical Paper 2000-01-0271 (2000). https://doi.org/10.4271/2000-01-0271.
- 28. Moshfeghian, M., "Correlations for Conversion between True and Reid Vapor Pressures," *Best Tips Of The Month* 20-28 (2018)
- 29. Liu, Y.-D., Jia, M., Xie, M.-Z., and Pang, B., "Enhancement on a Skeletal Kinetic Model for Primary Reference Fuel

- Oxidation by Using a Semidecoupling Methodology," *Energy Fuels* 26, no. 12 (2012): 7069-7083, doi:10.1021/ef301242b.
- Hu, J., Hall, M., Matthews, R., Moilanen, P. et al., "A Novel Technique for Measuring Cycle-Resolved Cold Start Emissions Applied to a Gasoline Turbocharged Direct Injection Engine," SAE Int. J. Adv. & Curr. Prac. in Mobility 2, no. 5 (2020): 2469-2478. https://doi.org/10.4271/2020-01-0312.
- 31. Groff, E.G. and Matekunas, F.A., "The Nature of Turbulent Flame Propagation in a Homogeneous Spark-ignited Engine," SAE Technical Paper 800133 (1980). https://doi.org/10.4271/800133.

Contact Information

Prof. Matthew J. Hall,

The University of Texas at Austin, Department of Mechanical Engineering, 204 E. Dean Keeton St. C2200, Austin, TX 78712,

USA

mjhall@mail.utexas.edu

Acknowledgments

This project was made possible through the funding provided by the Ford Motor Co. through the University of Texas at Austin's Site of the NSF Center for Efficient Vehicles and Sustainable Transportation Systems (EV-STS).

We wish to thank CONVERGE CFD™ for providing us with licenses for their simulation software and for their generous technical support.

Definitions/Abbreviations

ABDC - After bottom dead center

AMR - Adaptive mesh refinement

ATDC - After top dead center

BBDC - Before bottom dead center

BDC - Bottom dead center

BTDC - Before top dead center

CAD - Crank angle degrees

CFD - Computational fluid dynamic

DISI - Direct injection spark ignition

ECU - Engine control unit

EVC - Exhaust valve closing

EVO - Exhaust valve opening

FRP - Fuel rail pressure

FTP - Federal Test Procedure

GDI - Gasoline direct injection

GTDI - Gasoline turbocharged direct injection

HC - Hydrocarbons

A SIMULATION STUDY ON THE TRANSIENT BEHAVIOR OF A GASOLINE DIRECT INJECTION ENGINE

IVC - Intake valve closing

IVO - Intake valve opening

MFB - Mass fraction burnt

PFI - Port-fuel injection

RANS - Reynold-averaged Navier-Stokes

RPM - Revolutions per minute

RVP - Reid vapor pressure

SMD - Sauter mean diameter

TDC - Top dead center

TVP - True vapor pressure

^{© 2022} SAE International. All rights reserved. No part of this publication may be reproduced, stored in a retrieval system, or transmitted, in any form or by any means, electronic, mechanical, photocopying, recording, or otherwise, without the prior written permission of SAE International.